Spatial Coherence Properties of Organic Molecules Coupled to Plasmonic Surface Lattice Resonances in the Weak and Strong Coupling Regimes

L. Shi,[1] T. K. Hakala,[1] H. T. Rekola,[1] J.-P. Martikainen,[1] R. J. Moerland,[1,2] and P. Törmä[1,*]

[1] *COMP Centre of Excellence, Department of Applied Physics, Aalto University, FI-00076 Aalto, Finland*

[2] *Department of Imaging Physics, Faculty of Applied Sciences, Delft University of Technology, Lorentzweg 1, NL-2628 CJ, Delft, The Netherlands*

We study spatial coherence properties of a system composed of periodic silver nanoparticle arrays covered with a fluorescent organic molecule (DiD) film. The evolution of spatial coherence of this composite structure from the weak to the strong coupling regime is investigated by systematically varying the coupling strength between the localized DiD excitons and the collective, delocalized modes of the nanoparticle array known as surface lattice resonances. A gradual evolution of coherence from the weak to the strong coupling regime is observed, with the strong coupling features clearly visible in interference fringes. A high degree of spatial coherence is demonstrated in the strong coupling regime, even when the mode is very excitonlike (80 %), in contrast to the purely localized nature of molecular excitons. We show that coherence appears in proportion to the weight of the plasmonic component of the mode throughout the weak-to-strong coupling crossover, providing evidence for the hybrid nature of the normal modes.

PACS numbers: 33.80.-b, 73.20.Mf, 42.50.Nn

arXiv:1404.4160v1 [physics.optics] 16 Apr 2014

Spatial coherence properties of waves can be probed by passing a wave front through distant slits and observing interference. Inspired by this phenomenon well known for classical radiation, interference experiments were crucial in establishing the wave-particle nature of single photons, as well as massive particles [1–3], within quantum mechanics. In the experiments [1–3] the quantum mechanical wave properties of matter became visible at low temperatures. Here, we consider a different question: the spatial coherence properties of objects, or modes, that are hybrids of wavelike and particlelike components. Mixing a localized matter component with light may possibly give the hybrid object a nontrivial spatial coherence length.

Examples of light-matter hybrids include coherent superpositions of atoms and cavity photons [4, 5], semiconductor cavity polaritons, which have been brought to quantum degeneracy and condensation [6], and cavity photon mediated strong coupling between spatially separated localized molecular excitons [7]. Recently, delocalized electromagnetic modes supported by metal surfaces (surface plasmon polaritons) or periodic arrays of metallic nanoparticles [surface lattice resonances (SLRs) [8–11]] have been shown to strongly couple with localized emitters [12–19]. The strong coupling in these plasmonic systems involves a large number N of emitters. The normal mode splittings observed are consistent both with classical linear dispersion theory and with the vacuum Rabi splitting obtained as the low excitation limit of the Dicke model, similarly to the early experiments on many atoms in cavities [20]. The collective behavior of many emitters has been clearly demonstrated in these systems, manifested as the $\sqrt{N}$ dependence of the splitting. The observed splittings in dispersions strongly support the interpretation that the new normal modes are hybrid modes formed by strong coupling of lightlike (the surface plasmon polariton/SLR) and matterlike (the molecular excitation) components. Observations of the dispersions alone, however, cannot directly test whether the new modes carry all the essential properties of the original modes, as should be the case if the hybrids are linear, coherent combinations of the original modes. In particular, spatial coherence is the specific characteristic of an extended light mode: in order to prove that the new modes carry this property, interference experiments are needed. To be conclusive, it is necessary to show that the coherence appears in proportion to the weight of the light mode in the hybrid. This in turn requires a systematic study of coherence throughout the weak-to-strong coupling crossover. This is the goal of the present work.

The spatial interference effects of light-matter hybrids have been studied in a few experiments in the context of exciton-polariton condensates [6, 21, 22]. In plasmonic systems, only one experiment has been reported [23]: signatures of coherence were observed in the strong coupling regime in a planar metal surface—molecular film system. However, that work does not prove the connection of the spatial coherence with the weight of the light component since there was no study of the weak-to-strong coupling crossover (a different system, namely quantum dots, was given as the weak coupling reference). Here, we study the spatial coherence properties of a system composed of periodic silver nanoparticle arrays covered with fluorescent organic molecules (DiD) by employing a double slit experiment. We gradually increase the molecule concentration to investigate both the strong and the weak coupling coherence properties within the same system.

Figure 1(a) shows a scanning electron micrograph (SEM) of a typical array (for fabrication details, see Supplemental Material [24]). The $d_y = 50$ nm, $p_y = 200$

nm, while d_x and p_x were varied between 133–400 nm and 380–500 nm, respectively. The DiD concentration in poly(methyl methacrylate) film was varied between 20–800 mM.

The measurement setup is depicted in Fig. 1(b). y-polarized white light was incident on the sample; see Fig. 1(a). Angle and wavelength-resolved transmission spectra $T = I_{\mathrm{Structure}}/I_{\mathrm{Reference}}$ [Fig. 1(b)] were measured and subsequently used for calculating the dispersion for each array. The entrance slit of the spectrometer and the in-plane wave vector k is parallel to the x axis of the sample with magnitude $k = 2\pi/\lambda \sin(\theta)$, where λ is the wavelength in the medium and θ is the angle between the optical axis and the light propagation direction.

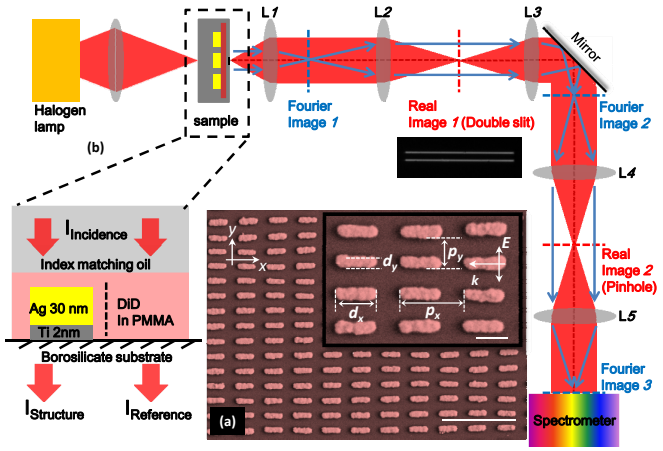

FIG. 1: (a) A SEM of a typical sample. The scale bar is 1 μm (200 nm for the inset). (b) The measurement setup. Angle resolved transmission spectra for each array were measured by placing the back focal plane of the sample at the entrance slit of the spectrometer. For spatial coherence measurements, a double slit was placed at the first intermediate image plane of the system.

In Figs. 2(a)–2(o) are shown the measured angle resolved extinction $(1-T)$ spectra for different nanoparticle arrays. Several observations can be made from these figures. First, the energy of the Γ point ($k = 0$) can be changed by changing the periodicity [see for example Figs. 2(a) and 2(k)]. Second, upon coupling of the <+1, 0> and <-1, 0> diffractive orders [25], a band gap is formed in Fig. 2(f) and the associated new modes can be made either dark or bright by changing the filling fraction [d_x/p_x, see Fig. 1(a)]. For details, see Supplemental Material [24].

The dispersions in Fig. 2(b)–2(e) illustrate how the system gradually evolves from the weak to the strong coupling regime with increasing molecular concentration. A clear modification of the system energies is observed in Figs. 2(b)–2(d), which then in Fig. 2(e) develops into a distinctive band bending and anticrossing at the energy corresponding to the absorption maximum of the molecule, a behavior that is characteristic for the strong coupling regime. Similar evolution from weak to strong coupling regime can readily be identified for arrays 2 [Figs. 2(f)–2(j)] and 3 [Figs. 2(k)–2(o)], but now the system energies are drastically different due to different filling fraction (array 2) and periodicity (array 3). These results demonstrate how the choice of geometry and molecular concentration provides excellent control over the system properties.

In the strong coupling theory, the new modes are linear combinations of the uncoupled SLRs and the molecular excitations. To describe such hybrid modes, we employ a coupled oscillator model satisfying the equation

$$\begin{pmatrix} E_{SLR}(k) + i\gamma_{SLR} & \Omega \\ \Omega & E_{DiD} + i\gamma_{DiD} \end{pmatrix} \begin{pmatrix} \alpha \\ \beta \end{pmatrix} = 0, \quad (1)$$

where E and γ are the energies and the widths of the uncoupled modes, Ω is the coupling strength between the SLR and DiD, and α and β are the coefficients of the linear combination of SLR and the DiD exciton (for details see Supplemental Material [24]). The SLR-exciton coupling strength Ω and the linewidth γ_{DiD} of the exciton are used as fitting parameters. The resulting mode energies are plotted in Figs. 2(c)–2(e), 2(h)–2(j), and 2(m)–2(o) for different arrays and are in good agreement with the experimentally observed mode energies. The SLR-exciton coupling is expected to scale as $\sqrt{N/V}$, where N is the number of molecules and V is the mode volume [26, 27]: this is confirmed in Fig. 2(p). Notably, the size of the observed splitting is in reasonable agreement with microscopic theory [26] (see Supplemental Material [24]). Note that spectrally broad emitters coupled to spectrally selective (plasmon) modes can produce luminescence spectra reminiscent of those observed in strongly coupled systems (see, e.g., Ref. [28]). That we observe strong coupling instead of this phenomenon is proven by the series of different concentrations that we studied, showing the $\sqrt{N/V}$ dependence expected for strong coupling.

In Figs. 2(q)–2(s), we plot the relative weights of the hybrid modes as functions of the in-plane wave vector k for arrays 1–3, respectively, with molecular concentrations of 200, 400, and 800 mM. For arrays 1 and 2, the SLR-exciton hybrid is mostly SLR-like for $k \sim 0$, and becomes increasingly excitonlike for higher k values. The relative exciton contribution at $k \sim 0$ increases with concentration due to stronger hybridization of the SLR with the exciton. Note, however, that for array 3 [Fig. 2(s)] the mode is excitonlike at $k \sim 0$, and then gradually evolves to SLR-like mode at higher k. This is due to the SLR Γ-point energy being above the molecular excitation energy [compare, for example, Figs. 2(g) and 2(l)). These results demonstrate how the relative weights of the hybrid mode at a given energy and wave vector can be tailored by choice of geometry and molecular concentration.

To investigate coherence, angle resolved transmission spectra are recorded with a double slit placed on the

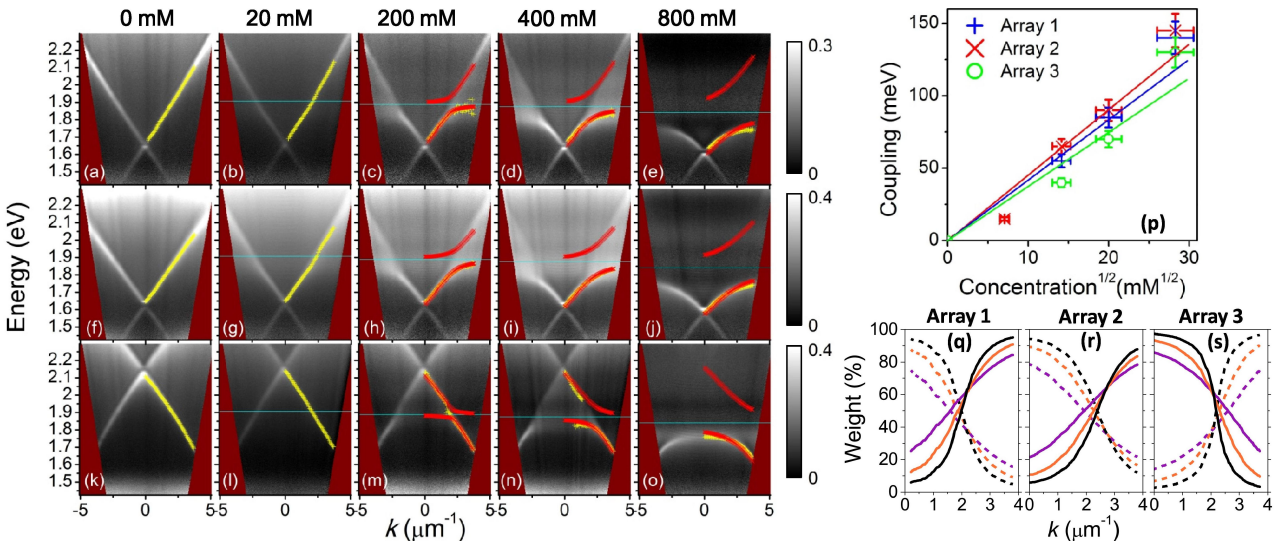

FIG. 2: The dispersions of three different nanoparticle arrays with inreasing DiD concentration. (a)–(e) Array 1, $(d_x) \times (d_y)$ = 50 nm × 220 nm, p_x = 500 nm. (f)–(j) Array 2, $(d_x) \times (d_y)$ = 50 nm × 355 nm, p_x = 500 nm. (k)–(o) Array 3, $(d_x) \times (d_y)$ = 50 nm × 167 nm, p_x = 380 nm. The first column corresponds to a case without DiD molecules, while the second, third, fourth, and fifth columns have 20, 200, 400, and 800 mM concentrations of DiD, respectively. White areas correspond to maximum extinction. The blue horizontal lines depict the absorption maximum of the DiD film. The yellow lines correspond to peak positions obtained from fitting a Gaussian curve to the line cuts of dispersions while keeping k constant, and the red lines are obtained from the coupled oscillator model. (p) The SLR-exciton coupling strength as a function of square root of concentration. The blue plus signs, red crosses, and green circles correspond to arrays 1, 2 and 3, respectively. (q)-(s) The relative SLR-exciton weights of the arrays 1-3, respectively. The solid (dashed) line corresponds to exciton (SLR) percentage and black, orange and purple to concentrations of 200, 400, and 800 mM, respectively.

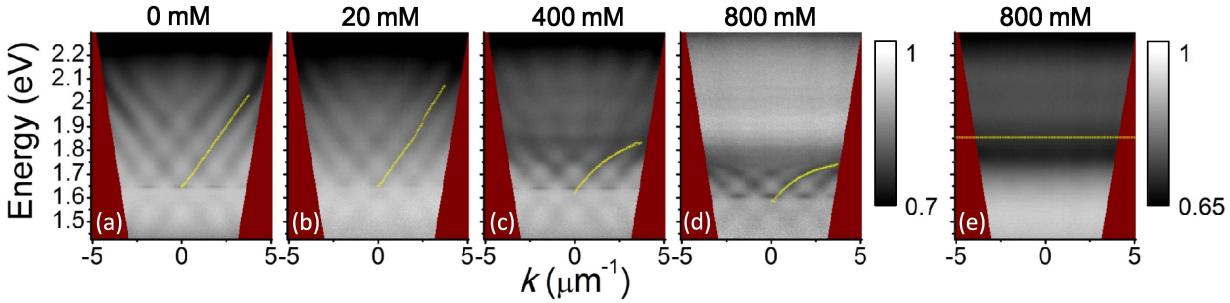

FIG. 3: (a)–(d) The spatial coherence images for the array 2 with concentrations 0, 20, 400, and 800 mM, respectively. Here white areas correspond to transmission maximum. The yellow lines have the same meaning as in Fig. 2. (e) A sample having a random distribution of nanoparticles with 800 mM DiD concentration. Two transmission minima are seen at 1.85 eV (yellow line) and 2.25 eV, corresponding to DiD absorption and the single particle plasmon resonance, respectively.

image plane of the sample; see Fig. 1(b). This forms the crucial test for the presence of spatial coherence in the new modes: if the spatial coherence length of the mode is greater than the interslit distance, a distinctive fringe pattern would be expected in the Fourier plane of the imaging system. In Fig. 3(a)–3(d) are shown the wavelength-resolved spatial coherence images obtained from array 2 and with molecular concentrations ranging from 0 to 800 mM. Intriguingly, *bending of the interference pattern* is observed towards the strong coupling regime. In other words, one of the destructive interference fringes in spatial coherence images always overlaps with the extinction maxima of the dispersion (yellow symbols); see Figs. 2(g)-2(j). This allows to make an important connection with the original modes: If a spatially coherent light source (i.e., the sample) is radiating through a double slit, the interference fringes can be interpreted as replicas of the original dispersion (Fig. 2) created by the diffracted orders from the double slit. At high frequencies the interference pattern becomes complex due to the close spacing of the crossing points of the replicas (see also Supplemental Material [24]). Thus, the fact that band bending with increasing concentration is seen both in the dispersions and the spatial coherence

images provides a clear signature that the interference fringes are directly related to the modes of interest and are not due to any secondary reason. We have thus conclusively shown that the system modes have prominent spatial coherence throughout the crossover, also deep in the strong coupling regime.

We want to point out the important role of the array periodicity, i.e the existence of the dispersive SLR modes, for the emergence of long-range coherence. Figure 3(e) shows a spatial coherence image of a sample having a random interparticle spacing (for a SEM image, see Supplemental Material [24]) while the molecular concentration, nanoparticle size, orientation and number are the same as in the sample in Fig. 3(d). Evidently, no interference fringes are present in this case. Also, they are absent in DiD films without nanoparticles.

Notably, the fringes become less visible with increasing concentration at energies above 1.8 eV; see Figs. 3(b)–3(d). Higher molecular concentration induces stronger hybridization between the delocalized SLR and localized molecular excitons. At higher energies, these hybrid modes become increasingly excitonlike and localized as the energy gets closer to DiD dye absorption, reducing the spatial coherence length below the interslit distance. Note, however, that the fringe pattern persists below 1.8 eV energies, even with 800 mM concentration. We have thus demonstrated that the SLR-exciton hybrid modes display long-range coherence even when the mode is very excitonlike: from Fig. 2(r) the exciton weight can be deduced to be 80% at high k-vector values.

In the rest of this Letter, we consider the crucial question of whether there is a systematic, quantitative connection between the spatial coherence and the expected weight of the light component in a hybrid mode. First, we want to show that detailed structure of the interference fringes can be produced by assuming hybrid modes, with weights of the light and matter parts as obtained by fitting the experimental dispersion with the coupled oscillator model Eq. (1) (the obtained dispersion was then used to provide the energy and wave vector specific information of the mode radiating through the double slit, see Supplemental Material [24]). In Fig. 4(a) we show a close-up of the spatial coherence image of Fig. 3(d) (800 mM concentration) and in Fig. 4(b) we show the interference image obtained from calculations based on the coupled oscillators model. While the intensities in both Figs. 4(a) and 4(b) are of comparable magnitude, at high energies, the experimental data have less transmission intensity. This can be due to additional absorption of the molecules that are not contributing to strong coupling [12, 26]. In general, however, the correspondence of the model with the most prominent features of the experimental data is excellent. This is the first step of systematically proving the connection between the hybrid structure and the coherence: the model with weights of matter and light parts in the hybrid as given by strong coupling theory indeed reproduces the interference pattern observed experimentally.

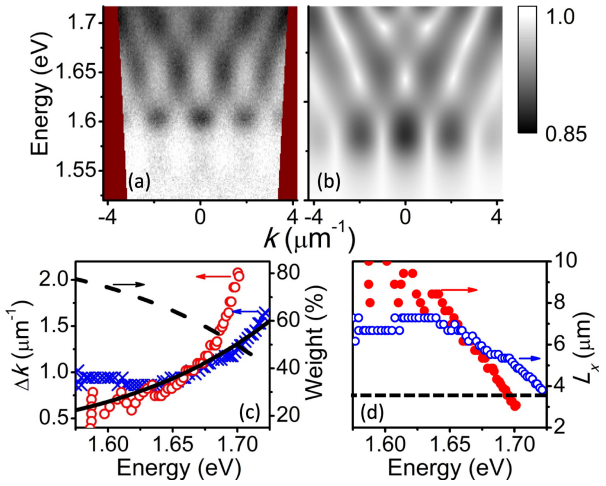

FIG. 4: (a) A close-up of the spatial coherence image (800 mM concentration). (b) The interference image obtained from the coupled oscillator model. (c) The Δk obtained from the experiments (red empty circles) and from the coupled oscillator model (blue crosses). Dashed and solid lines correspond to the SLR and exciton weights of the mode, respectively. (d) The spatial coherence length obtained from the experiments (red circles) and from the coupled oscillator model (blue empty circles). The dashed line is the effective interslit distance at the sample plane.

Second, we consider the important connection between the interference fringes, mode delocalization, the width of the mode Δk, and the relative weights of the strongly coupled modes. In Fig. 4(c) we show the Δk of the mode as a function of the energy obtained from the experiments (Fig. 2) and from the model. The Δk was obtained as FWHM of constant-energy line cuts from the dispersions. Also shown are the relative SLR and exciton weights of the hybrid mode. In Fig. 4(d) we show the spatial coherence lengths of the mode obtained as $L_x = 2\pi/\Delta k$ [29]. Because the momentum and position are Fourier related, a small Δk at energies around 1.6 eV [see Fig. 4(c)] suggests a delocalized mode and large spatial coherence length. The delocalization is also evident from the high SLR fraction (80 %) of the mode. In the spatial coherence image, the delocalization manifests itself as a distinct interference pattern [Figs. 4(a) and 4(b)]. As Δk increases at energies $E > 1.65$ eV, however, the hybrid mode becomes more localized and more excitonlike, which gradually yields a less prominent interference pattern in accordance with the increasing weight of the matter component. At energies above 1.7 eV, the spatial coherence length decreases below the interslit distance [Fig. 4(d)], and, consequently the interference pattern disappears; see Fig. 3(d).

In both classical optics and quantum mechanics, modes are characterized not only by their energies, observable in

dispersions, but also by the coherent modes or wave functions forming linear superpositions. Both aspects should be considered in identifying physical phenomena, cf. the observation of Bose-Einstein condensation by evidence in momentum distribution [30] and in interference patterns [31]. The strong coupling regime of various types of surface plasmon modes and emitters has been widely studied by observing dispersion relations. Splittings in the dispersions have been attributed to hybridization of plasmonic and excitonlike modes. Here we provide the first systematic study of the evolution of the spatial coherence in a plasmonic-molecule system when transiting from the weak to the strong coupling regime. The evolution of spatial coherence is shown to be directly connected to the hybrid mode structure. Significant spatial coherence lengths in the strongly coupled system are observed even when the mode is very excitonlike. Complementing the energy dispersions and dynamics observed earlier, our interference results provide conclusive evidence for the hybrid nature of the normal modes in strongly coupled surface plasmon—emitter systems. In general, our results demonstrate the potential of hybridization in creating nanosystems with designed properties, in this case long range coherence for modes that are largely matterlike.

We thank Dr. Shaoyu Yin for useful discussions. This work was supported by the Academy of Finland through its Centres of Excellence Programme (Projects No. 251748, No. 263347, No. 135000, and No. 141039) and by the European Research Council (ERC-2013-AdG-340748-CODE). Part of the research was performed at the Micronova Nanofabrication Centre, supported by Aalto University.

* Electronic address: paivi.torma@aalto.fi

[1] C. Davisson and L. H. Germer, Phys. Rev. **30**, 705 (1927).
[2] M. Arndt, O. Nairz, J. Vos-Andreae, C. Keller, G. van der Zouw, and A. Zeilinger, Nature (London) **401**, 680 (1999).
[3] T. Juffmann, A. Milic, M. Mullneritsch, P. Asenbaum, A. Tsukernik, J. Tuxen, M. Mayor, O. Cheshnovsky, and M. Arndt, Nat. Nanotechnol. **7**, 297 (2012).
[4] G. Rempe, H. Walther, and N. Klein, Phys. Rev. Lett. **58**, 353 (1987).
[5] R. J. Thompson, G. Rempe, and H. J. Kimble, Phys. Rev. Lett. **68**, 1132 (1992).
[6] J. Kasprzak, M. Richard, S. Kundermann, A. Baas, P. Jeambrun, J. M. J. Keeling, F. M. Marchetti, M. H. Szymanska, R. Andre, J. L. Staehli, *et* al., Nature (London) **443**, 409 (2006).
[7] D. G. Lidzey, D. D. C. Bradley, A. Armitage, S. Walker, and M. S. Skolnick, Science **288**, 1620 (2000).
[8] S. Zou, N. Janel, and G. C. Schatz, J. Chem. Phys. **120**, 10871 (2004).
[9] F. J. García de Abajo, Rev. Mod. Phys. **79**, 1267 (2007).
[10] B. Auguié and W. L. Barnes, Phys. Rev. Lett. **101**, 143902 (2008).
[11] W. Zhou, M. Dridi, J. Y. Suh, C. H. Kim, D. T. Co, M. R. Wasielewski, G. C. Schatz, and T. W. Odom, Nat. Nanotechnol. **8**, 506–511 (2013).
[12] J. Bellessa, C. Bonnand, J. C. Plenet, and J. Mugnier, Phys. Rev. Lett. **93**, 036404 (2004).
[13] J. Dintinger, S. Klein, F. Bustos, W. L. Barnes, and T. W. Ebbesen, Phys. Rev. B **71**, 035424 (2005).
[14] T. K. Hakala, J. J. Toppari, A. Kuzyk, M. Pettersson, H. Tikkanen, H. Kunttu, and P. Törmä, Phys. Rev. Lett. **103**, 053602 (2009).
[15] D. E. Gomez, K. C. Vernon, P. Mulvaney, and T. J. Davis, Nano Lett. **10**, 274 (2010).
[16] T. Schwartz, J. A. Hutchison, C. Genet, and T. W. Ebbesen, Phys. Rev. Lett. **106**, 196405 (2011).
[17] P. Vasa, W. Wang, R. Pomraenke, M. Lammers, M. Maiuri, C. Manzoni, G. Cerullo, and C. Lienau, Nat. Photonics **7**, 128 (2013).
[18] S. R. K. Rodriguez and J. Gomez Rivas, Opt. Express **21**, 27411 (2013).
[19] A. I. Väkeväinen, R. J. Moerland, H. T. Rekola, A.-P. Eskelinen, J.-P. Martikainen, D.-H. Kim, and P. Törmä, Nano Lett., **14**, 1721 (2014).
[20] Y. Zhu, D. J. Gauthier, S. E. Morin, Q. Wu, H. J. Carmichael, and T. W. Mossberg, Phys. Rev. Lett. **64**, 2499 (1990).
[21] M. Richard, J. Kasprzak, R. Romestain, R. André, and L. S. Dang, Phys. Rev. Lett. **94**, 187401 (2005).
[22] H. Deng, G. S. Solomon, R. Hey, K. H. Ploog, and Y. Yamamoto, Phys. Rev. Lett. **99**, 126403 (2007).
[23] S. Aberra Guebrou, C. Symonds, E. Homeyer, J. C. Plenet, Y. N. Gartstein, V. M. Agranovich, and J. Bellessa, Phys. Rev. Lett. **108**, 066401 (2012).
[24] See Supplemental Material at the end of this document, which also includes Refs. [26, 27 and 32] for additional sample fabrication details, strong coupling theory and additional details about the double slit experiments.
[25] W. L. Barnes, T. W. Preist, S. C. Kitson, and J. R. Sambles, Phys. Rev. B **54**, 6227 (1996).
[26] V. M. Agranovich, M. Litinskaia, and D. G. Lidzey, Phys. Rev. B **67**, 085311 (2003).
[27] A. González-Tudela, P. A. Huidobro, L. Martín-Moreno, C. Tejedor, and F. J. García-Vidal, Phys. Rev. Lett. **110**, 126801 (2013).
[28] C. Gruber, A. Trügler, A. Hohenau, U. Hohenester, and J. R. Krenn, Nano Lett. **13**, 4257 (2013).
[29] L. Mandel and E. Wolf, Rev. Mod. Phys. **37**, 231 (1965).
[30] M. H. Anderson, J. R. Ensher, M. R. Matthews, C. E. Wieman, and E. A. Cornell, Science **269**, 198 (1995).
[31] M. R. Andrews, C. G. Townsend, H.-J. Miesner, D. S. Durfee, D. M. Kurn, and W. Ketterle, Science **275**, 637 (1997).
[32] R. A. L. Vallée, M. Van Der Auweraer, F. C. De Schryver, D. Beljonne, and M. Orrit, ChemPhysChem **6**, 81-91 (2005).

Spatial Coherence Properties of Organic Molecules Coupled to Plasmonic Surface Lattice Resonances in the Weak and Strong Coupling Regimes

Supplemental Material

L. Shi, T. K. Hakala, H. T. Rekola, J. -P. Martikainen, R. J. Moerland, and P. Törmä

COMP Centre of Excellence, Department of Applied Physics, Aalto University, FI-00076 Aalto, Finland

The fabrication of the nanoparticle arrays and the absorbance of the bare DiD dye film

In Fig. 1 are shown the scanning electron micrographs (SEM) of a typical periodic and a random nanoparticle sample. The nanoparticle orientation, size and number were equal for both samples. The samples were fabricated with electron beam lithography and metal evaporation (Ti 2 nm / Ag 30 nm) on a borosilicate substrate. Several 40µm x 40µm arrays were fabricated with different particle lengths d and periodicities p, see Fig. 1(a) of the manuscript. The d_y = 50 nm for all the particles while d_x was varied from 133 nm to 400 nm for different arrays. Also, p_y was kept constant (200 nm) while p_x was systematically varied between 380-500 nm. The DiD molecules were mixed with poly(methyl methacrylate)–anisole solution and the resulting mixture was then spun cast onto the samples resulting to DiD concentrations from 20 mM to 800 mM in the film. Prior to the measurements, the sample was covered with index matching oil and another borosilicate slide to provide a symmetric refractive index environment.

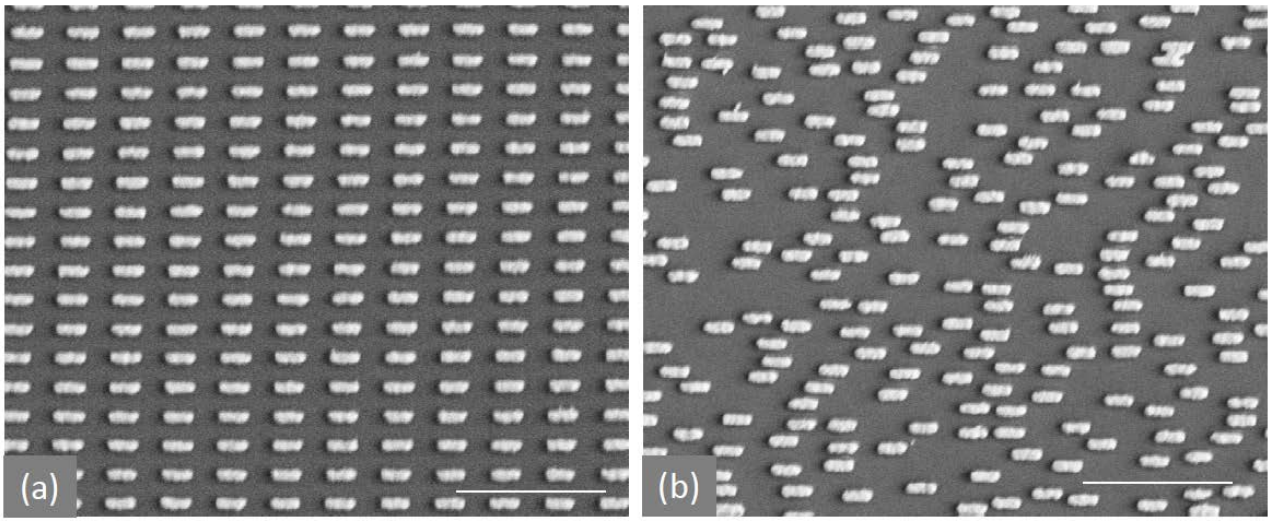

Fig. 1. SEM of a typical nanoparticle array (a) and a random sample (b). The scale bars are 1 μm.

The effect of increasing filling fraction: Bright and dark modes

The coupling of <+1, 0> and <-1, 0> diffractive orders in periodic structures leads to formation of a band gap. By changing the filling fraction either of the modes can be made dipole active. This can be seen in Fig. 2, where the extinction data is plotted for 6 different arrays with increasing filling fraction d_x / p_x. No DiD film was present in this case. The periodicity p_x = 460 nm, p_y = 200 nm and d_y = 50 nm for all the arrays, while the d_x was varied from 161 nm to 368 nm.

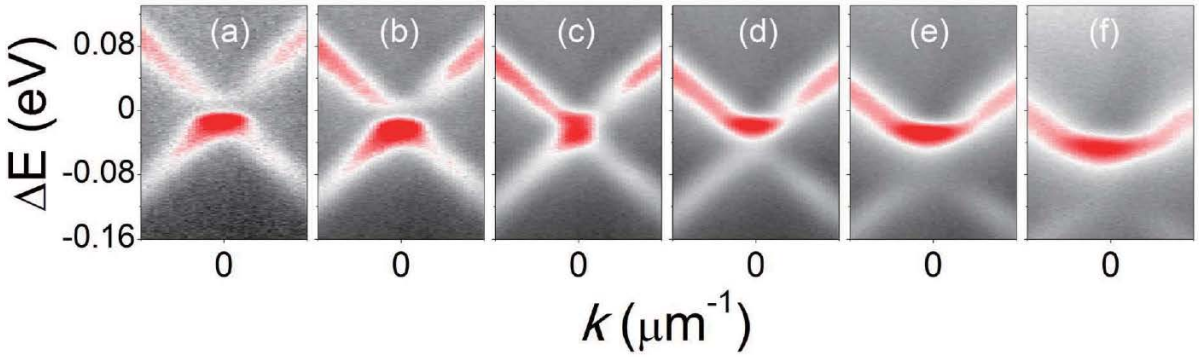

Fig. 2. The effect of increasing filling fraction d_x / p_x (see manuscript Fig. 1(a)) from 35 % to 80 % (in steps of 9%). The extinction maximum shifts from the lower energy branch to the higher energy one. The red (black) color corresponds to the highest (lowest) extinction.

DiD dye absorption

In Fig. 3 are shown the measured absorption curves from DiD films with various concentrations. Also shown are the two Gaussians and their sum fitted to the absorption curves in order to find the center energies for DiD film absorption at each concentration. These energies were then used as uncoupled DiD absorption energies in the coupled oscillator model.

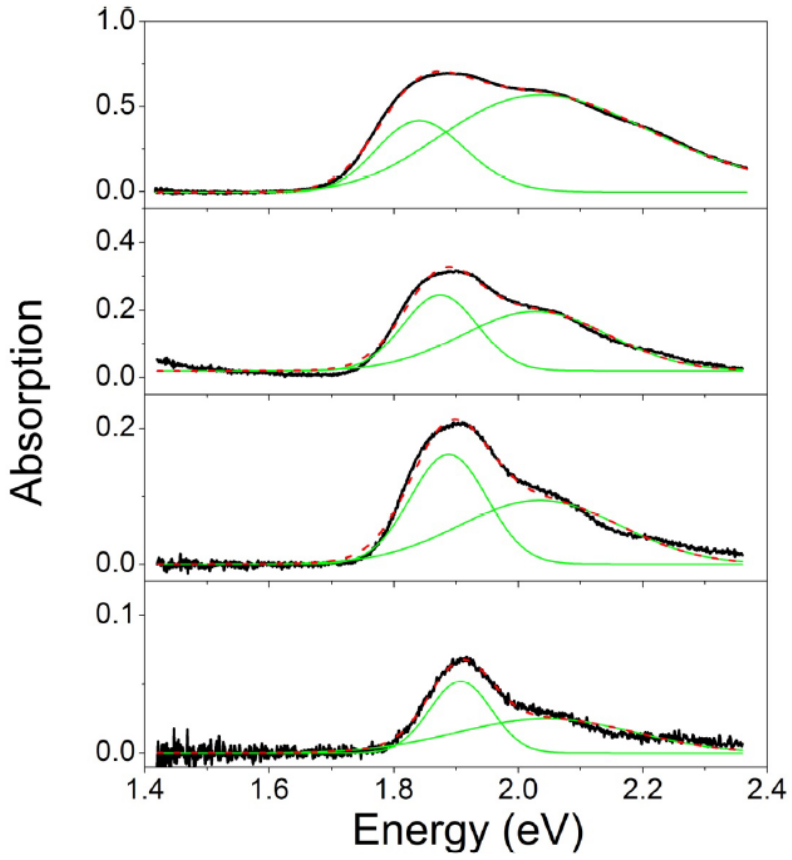

Fig. 3. The measured absorption curves (from top to bottom) for the DiD films with concentrations 800 mM, 400 mM, 200 mM, and 50 mM, respectively. Also shown are the two fitted Gaussians (green solid lines) and their sum (dashed red line).

Obtaining the *E*, γ and Δk from the measured extinction curves

From the measured dispersion data, the mode energy *E* (the peak of the red solid curve, see Fig. 4) and the width γ (FWHM of the red solid curve) were obtained for each *k*. The mode energies were then plotted as yellow symbols in Fig. 2 and 3 in the manuscript. As in [1], γ was then used to define the uncertainty in the parallel wavevector Δk, see Fig. 4.

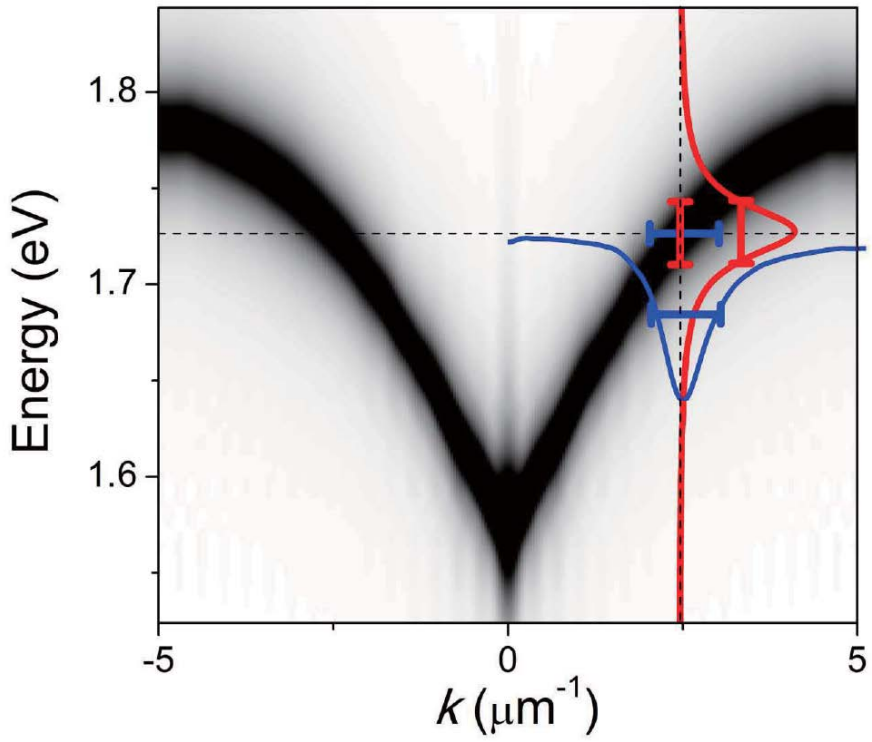

Fig. 4. The mode energy *E(k)* (the peak of the red solid curve) and the width γ (FWHM of the red solid curve) were obtained from the measured extinction data for each *k*.

Obtaining the relevant parameters for the coupled oscillator model

The parameters for the coupled oscillator model (See Eq. (1) of the manuscript) were obtained as follows. The energy $E_{SLR}(k)$ and the width γ_{SLR} of the uncoupled SLR mode were obtained from the measurements without the DiD film for each array, and the uncoupled DiD absorption energies E_{DiD} were obtained from the transmission measurements of the bare DiD film without any nanoparticles, see Fig. 3. For fitting, the SLR-DiD coupling strength Ω and the width of the DiD absorption γ_{DiD} were used as free parameters. Obtained by diagonalization of the matrix in Eq. 1 of the manuscript, the resulting hybrid mode eigenenergies were plotted as red symbols in Fig. 2 (c-e), (h-j) and (m-o) in the manuscript. Note that for 20 mM and 50 mM DiD concentration, the eigenenergies were essentially the same as in the absence of the dye, so the fitting resulted to negligible coupling strength (see Figs. 7-9 in the Supplemental Information and Fig. 2(p) in the manuscript). For the same reason, the obtained relative SLR-exciton weights are plotted only for the three largest DiD concentrations (200 mM, 400 mM and 800 mM) in Fig.2(q-s) in the manuscript.

Comparison between microscopic theory and experimental results

To estimate the size of the splitting in dispersions from first principles, we employ the light-matter strong coupling theory (see e.g. [1, 2]). Here, we directly quote the results given in reference [1], using corresponding microscopic quantities in our system. Accounting for a random orientation of the dye molecules in the system, the final coupling strength $\boldsymbol{\Omega}$ can be calculated as $\Omega = \sqrt{\Omega_0^2 - (\frac{\gamma_{SLR}^2 + \gamma_{DiD}^2}{2})} = \sqrt{\frac{d^2 E_{DiD}^2}{4\varepsilon_0 \varepsilon_b E_{SLR}(0)} \times \frac{N}{V_{SLR}} - (\frac{\gamma_{SLR}^2 + \gamma_{DiD}^2}{2})}$, where d is the intrinsic transition dipole moment of a single DiD molecule, $\boldsymbol{\varepsilon}_b$ is the relative permittivity of the background material, N is the number of the molecules enclosed by the optical field of the SLR and V_{SLR} is the mode volume of the SLR.

In Fig. 5, we compare our experimental results with the microscopic model. We would like to emphasize that, to the best our knowledge, this is the first (or at least one of the first) report(s) where a detailed comparison between experimentally observed splittings and microscopic predictions is made. The experimental results are the same as the data shown in the manuscript. In Fig. 5(a), the results from the microscopic model are calculated by directly using the values of the intrinsic dipole moment and the concentration of the DiD dye from the literature and our experiments without any further fitting parameters. The intrinsic dipole moment of a single DiD molecule is reported to be approximately $5*10^{-29}$ Cm [3]. The E_{DiD}, E_{SLR}, γ_{DiD} and γ_{SLR} are obtained from the experimental results of the uncoupled SLR dispersion and DiD absorption, shown in Fig. 2(a, f and k) of the manuscript and Fig. 2 in the Supplemental Information. The $\boldsymbol{\varepsilon}_b$ = 2.3. The $\frac{N}{V_{SLR}}$ equals the nominal concentration of the DiD dye in the polymer film. While the results from the microscopic model have the same linear dependence on the concentration as the experimental results, the obtained mode splitting is approximately 3 times higher. The discrepancy likely stems from various reasons, namely 1) the exact value of the dipole moment of the DiD molecule in our system may well be different from the value reported in [3], 2) in the experiments, only the top surface of the lattice structure is coated by the dye molecules, effectively reducing the magnitude of $\frac{N}{V_{SLR}}$ term, 3) the possible aggregation of the DiD molecules, leading to effectively lower concentration, is neglected in our model.

Next, we will, one by one, analyze the influences of the aforementioned aspects to the final coupling strength. First, if we leave the intrinsic dipole moment to be a free parameter, and using the experimental data to fit the intrinsic dipole moment, we obtain results are shown in Fig. 5(b). The obtained intrinsic dipole moment of a single DiD dye is $1.58*10^{-29}$ Cm, which is in the same order of the reported value [3] but approximately 3 times less. Second, approximately one half of the field of the SLR mode resides in the glass substrate where no DiD is present. Thus the value of $\frac{N}{V_{SLR}}$ could be naively estimated to be half of the nominal concentration of the DiD dye in the polymer film. Taking into account this fact, and still using the reported DiD dye intrinsic dipole moment ($5*10^{-29}$ Cm), we then obtain a coupling strength shown in Fig. 5(c). Obviously, the value is approaching the experimental results. Third, it is reasonable to assume that some of the DiD dye molecules aggregate in the polymer film, which results to the reduction of the effective DiD concentration. Despite the complexity of our system, it is interesting to find that there still exists a reasonable agreement between the results calculated from the first principles and the experimental data.

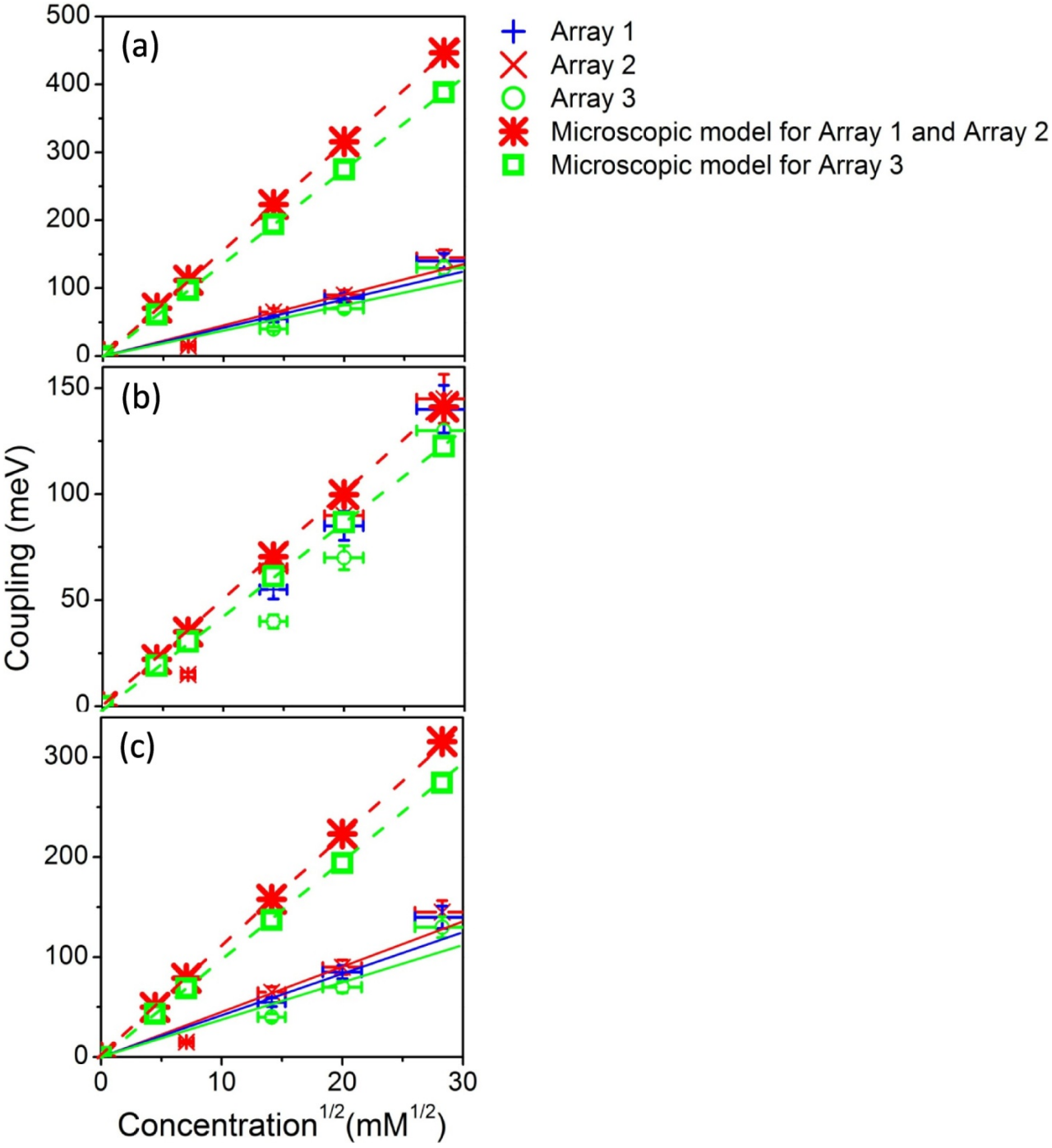

Fig. 5. The coupling strength obtained from microscopic model and experimental results. The symbols and their meaning are represented inside the figure. The experimental data shown here is the same as the Fig. 2(p) of the manuscript. The microscopic model results shown in (a and c) correspond to the case of $5*10^{-29}$ Cm intrinsic transition dipole moment of single DiD molecule, while (b) corresponds to the case of $1.58*10^{-29}$ Cm intrinsic transition dipole moment of single DiD molecule. In (a and b), the $\frac{N}{V_{SLR}}$ equal to the concentration of the DiD dye in the polymer film, and in (c), the $\frac{N}{V_{SLR}}$ equal to the half of the concentration of the DiD dye in the polymer film.

Generating the spatial coherence image from the coupled oscillator model

To generate the diffraction pattern from the coupled oscillator model (see Fig. 4(b) in the manuscript), the following procedure was applied: For every *k*, the eigenenergies *E(k)* and the widths γ of the strongly coupled mode were given by the real and imaginary parts of the diagonalized matrix (Eq. (1)), respectively. Then, for each *k,* we assumed a Lorentzian lineshape *f(E)*, whose center and width were given by *E(k)* and γ, respectively. These Lorentzians were used to construct a 2-D contour map *f(E, k)*, similar to experimentally obtained dispersion. This dispersion was then used to provide the energy and wavelength specific information of the mode radiating through the double slit.

By taking an inverse Fourier transform of the obtained dispersion *f(E, k)*, the real-space intensity distribution *f'(E, x)* of the mode at the position of the double slit was obtained for each *E*. The double slit transmission $\Phi(x)$ was assumed to be 1 at the slit openings and 0 elsewhere. The transmitted field $\Phi(x) \times f'(E, x)$ was then Fourier transformed to obtain the spatial coherence image.

Spatial coherence images with various double slit configurations

In Fig. 6 are shown the spatial coherence images in various slit configurations for the periodic structure (a, c and e) and for the random structure (b, d and f). Figs. 6(a) and (b) correspond to the experiments without double slit, (c) and (d) with double slit and (e) and (f) with one of the slits blocked so that only one slit is transmitting light. The concentration of the DiD is 800 mM. Note that in the absence of the double slit (Figs. 6(a) and (b)), the periodic structure displays a *k*-dependent dispersion, while the random structure shows two *k*-independent transmission minima at 1.8 eV and 2.25 eV, corresponding to DiD main absorption and single particle surface plasmon resonance, respectively. Note also an additional, very faint transmission minimum at around 2.05 eV in Fig. 6(b) that corresponds to the DiD absoption shoulder, see Fig. 3. By placing a double slit to the image plane of the sample, a distinct interference pattern is obtained from the periodic sample due to delocalized mode (Fig. 6 (c)), while the random sample maintains the two *k*-vector independent transmission minima. In the case of only single slit (Fig. 6(e)), the interference pattern from the periodic array disappears almost entirely. The mode delocalization is in this case limited by the effective slit width (3.5 μm), which effectively increases the Δk and reduces the interference effects. In contrast, the transmission of the sample with randomly distributed nanoparticles remains the same even in the presence of the single slit since the mode coherence length is smaller than the slit width, see Fig. 6(f).

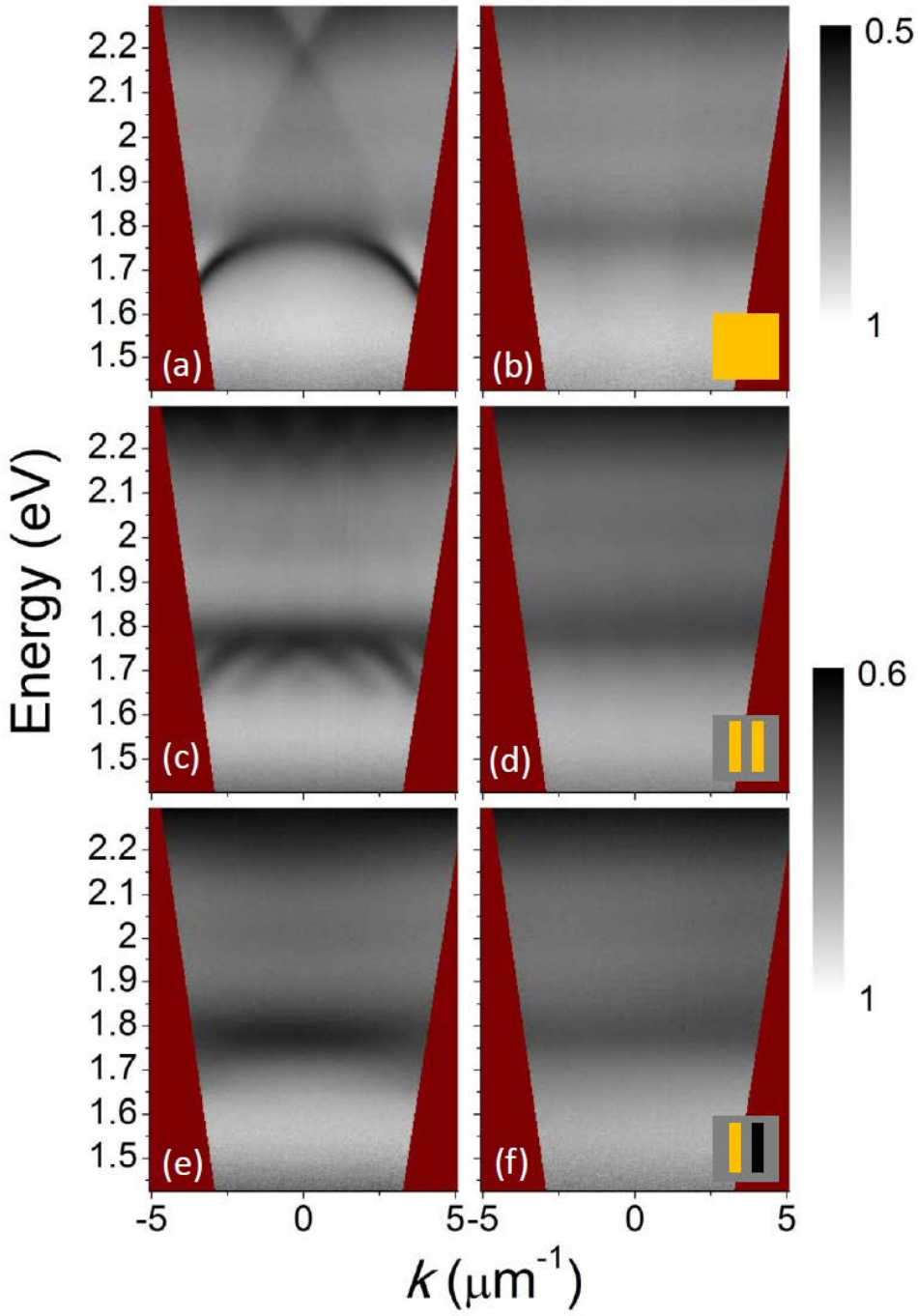

Fig. 6. The transmission intensities as functions of the parallel wavevector and the energy for the cases of the periodic structure (a, c and e) and the random structure (b, d and f). (a, b), (c, d) and (e, f) correspond to the experiments without double slit (shown inset of the (b)), with double slit (shown inset of the (d)) and with single slit (shown inset of the (f)) respectively. The concentration of the DiD is 800 mM. The periodic sample has dimensions d_x = 201 nm, d_y = 50 nm, p_x = 380 nm, p_y = 200 nm. Similar behavior can be seen for the array 3 in the manuscript which has approximately similar nominal dimensions (compare Fig. 6 (a) above to Fig. 2 (o) of the manuscript). In this case, the DiD exciton couples strongly with the *lower* energy branch of the SLR, while still maintaining the significant spatial coherence length as evidenced by the distinct interference pattern (see Fig. 6 (c) above).

The measured raw extinction data for various array dimensions and DiD concentrations

While the data in the manuscript is based on 3 different arrays for the sake of simplicity, altogether 24 different arrays with different dimensions were measured. We used 6 different molecular concentrations, 0 mM, 20 mM, 50 mM, 200 mM, 400 mM and 800 mM. The measured extinction data is shown in Figs. 7-12. Below are shown the dimensions for each array. Particle dimensions are in the form (d_x x d_y) and period dimensions in the form (p_x x p_y), see Fig. 1(a) in the manuscript. Note that the dimensions were chosen such that each *column* in Figs. 7-12 has the same filling fraction d_x / p_x while each *row* has the same periodicity p_x. The data is organized in such a way that a certain array always corresponds to the same letter (a, b, c, etc.). The white (black) color corresponds to the highest (lowest) extinction in all figures.

(a) 175.0x50.0 nm^2 particles with 500.0x200.0 nm^2 period

(b) 220.0x50.0 nm^2 particles with 500.0x200.0 nm^2 period

(c) 265.0x50.0 nm^2 particles with 500.0x200.0 nm^2 period

(d) 310.0x50.0 nm^2 particles with 500.0x200.0 nm^2 period

(e) 355.0x50.0 nm^2 particles with 500.0x200.0 nm^2 period

(f) 400.0x50.0 nm^2 particles with 500.0x200.0 nm^2 period

(g) 161.0x50.0 nm^2 particles with 460.0x200.0 nm^2 period

(h) 202.0x50.0 nm^2 particles with 460.0x200.0 nm^2 period

(i) 244.0x50.0 nm^2 particles with 460.0x200.0 nm^2 period

(j) 285.0x50.0 nm^2 particles with 460.0x200.0 nm^2 period

(k) 327.0x50.0 nm^2 particles with 460.0x200.0 nm^2 period

(l) 368.0x50.0 nm^2 particles with 460.0x200.0 nm^2 period

(m) 147.0x50.0 nm^2 particles with 420.0x200.0 nm^2 period

(n) 185.0x50.0 nm^2 particles with 420.0x200.0 nm^2 period

(o) 223.0x50.0 nm^2 particles with 420.0x200.0 nm^2 period

(p) 260.0x50.0 nm^2 particles with 420.0x200.0 nm^2 period

(q) 298.0x50.0 nm^2 particles with 420.0x200.0 nm^2 period

(r) 336.0x50.0 nm^2 particles with 420.0x200.0 nm^2 period

(s) 133.0x50.0 nm^2 particles with 380.0x200.0 nm^2 period

(t) 167.0x50.0 nm^2 particles with 380.0x200.0 nm^2 period

(u) 201.0x50.0 nm^2 particles with 380.0x200.0 nm^2 period

(v) 236.0x50.0 nm^2 particles with 380.0x200.0 nm^2 period

(w) 270.0x50.0 nm^2 particles with 380.0x200.0 nm^2 period

(x) 304.0x50.0 nm^2 particles with 380.0x200.0 nm^2 period

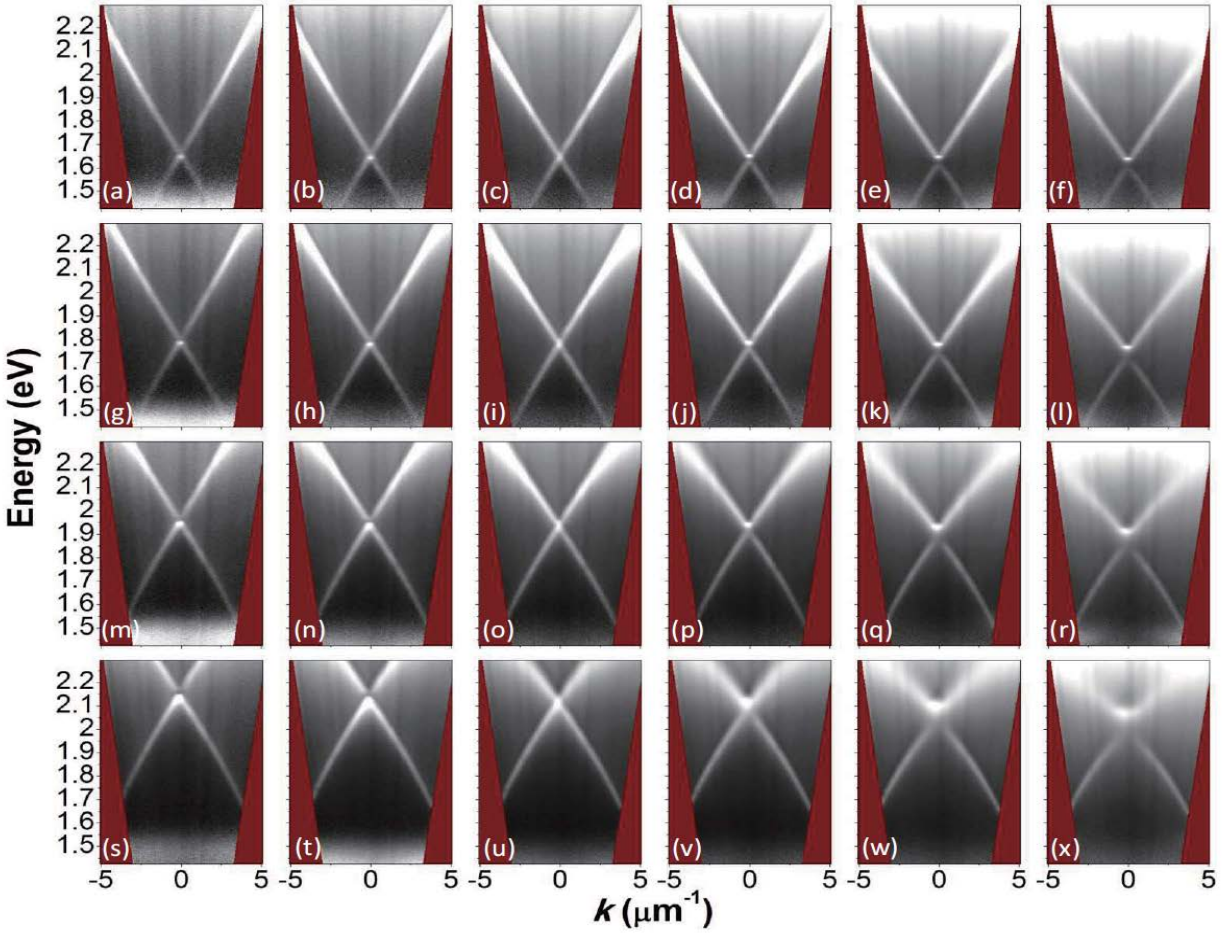

Fig. 7. The recorded raw extinction data for the arrays without any DiD film (0 mM case). The white (black) color corresponds to the highest (lowest) extinction.

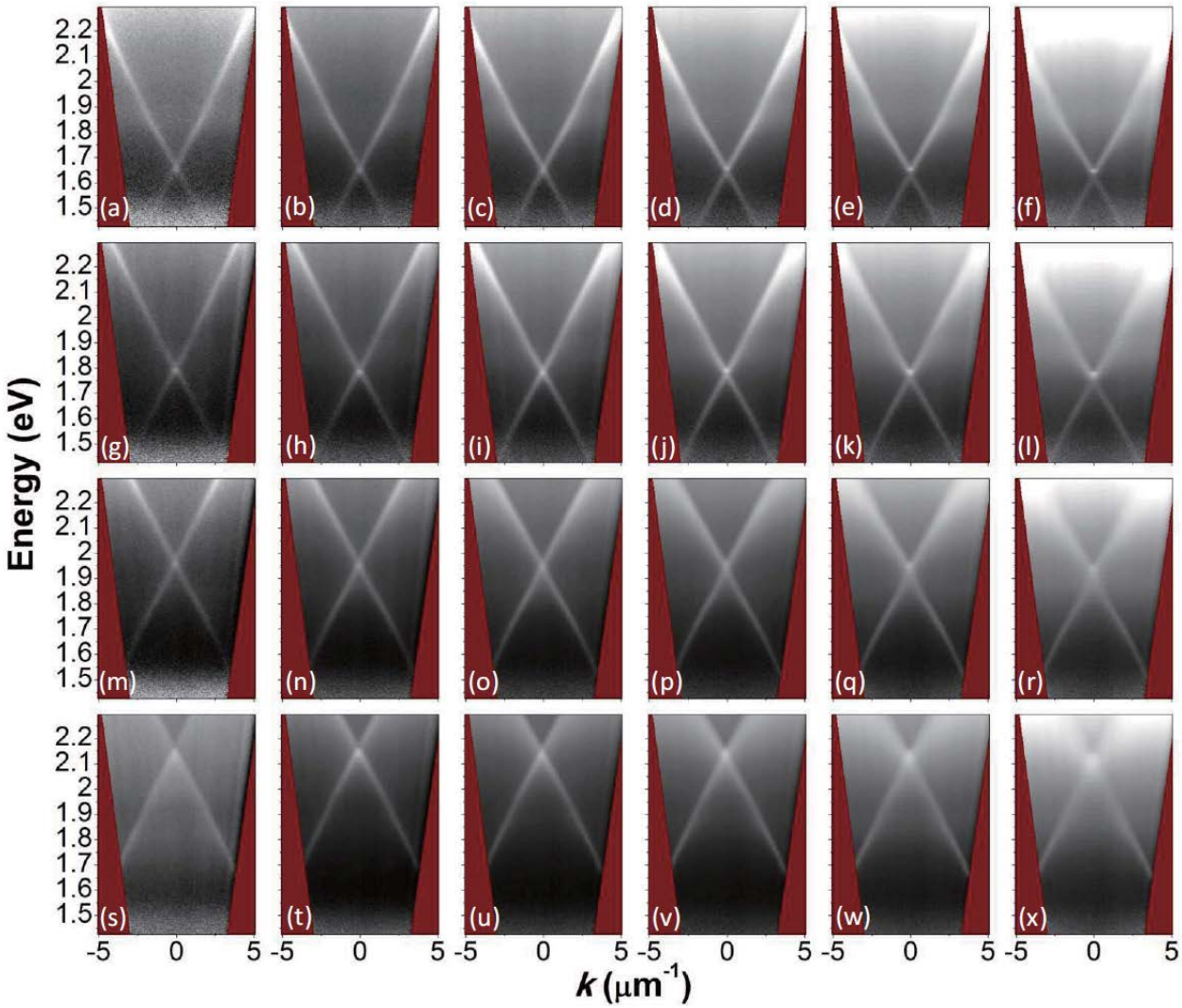

Fig. 8. The recorded raw extinction data for the arrays with 20 mM DiD concentration. The white (black) color corresponds to the highest (lowest) extinction.

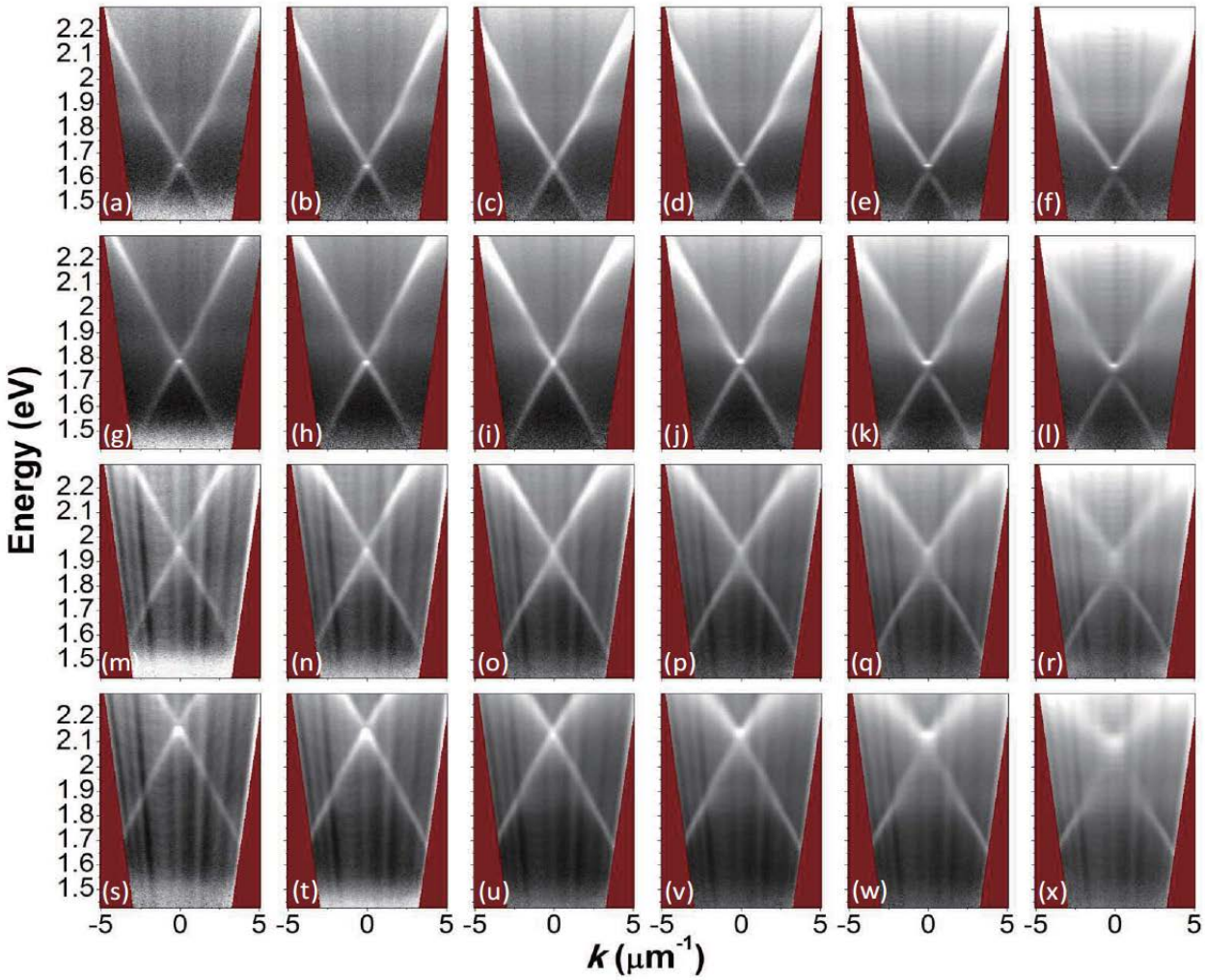

Fig. 9. The recorded raw extinction data for the arrays with 50 mM DiD concentration. The white (black) color corresponds to the highest (lowest) extinction.

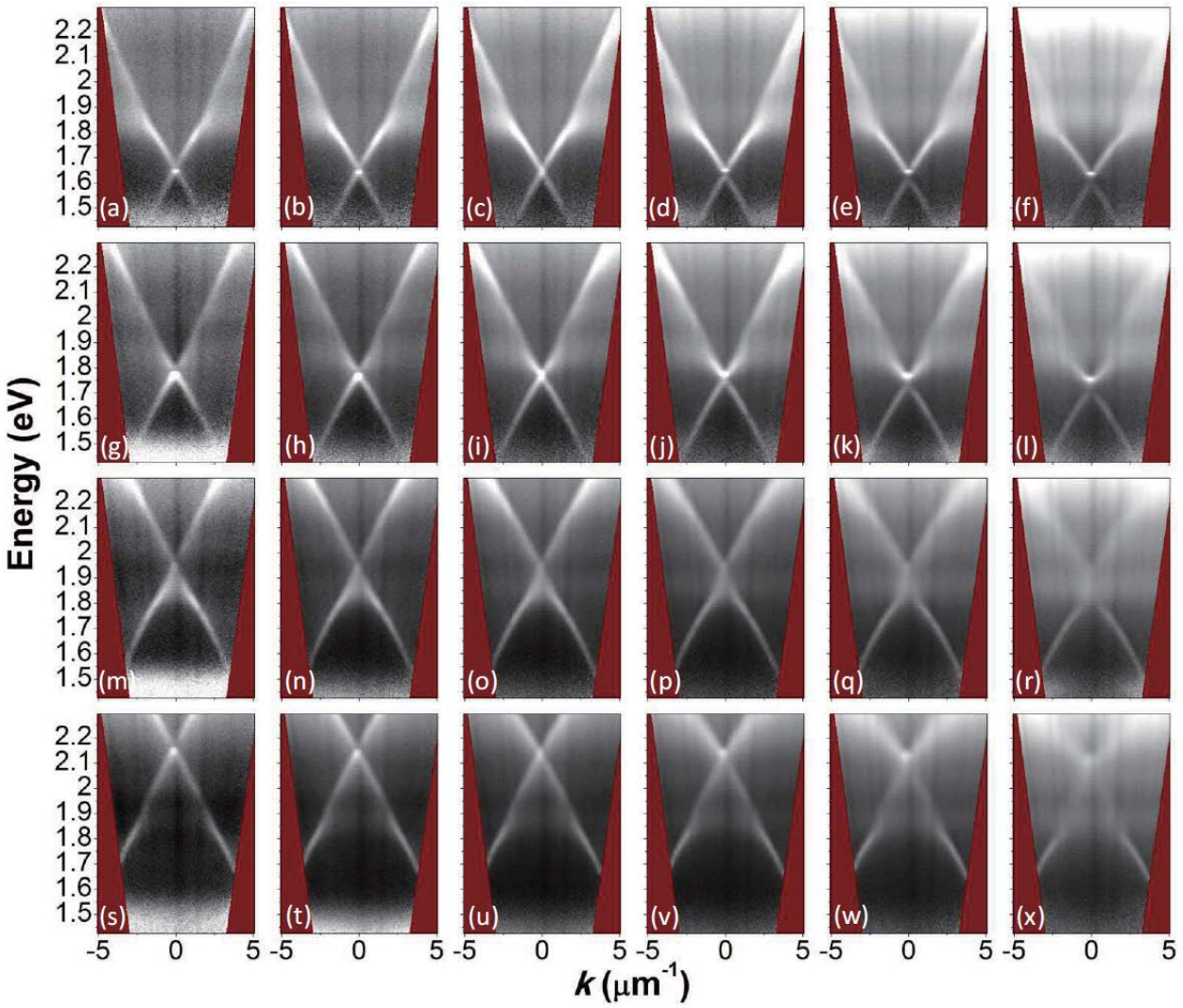

Fig. 10. The recorded raw extinction data for the arrays with 200 mM DiD concentration. The white (black) color corresponds to the highest (lowest) extinction.

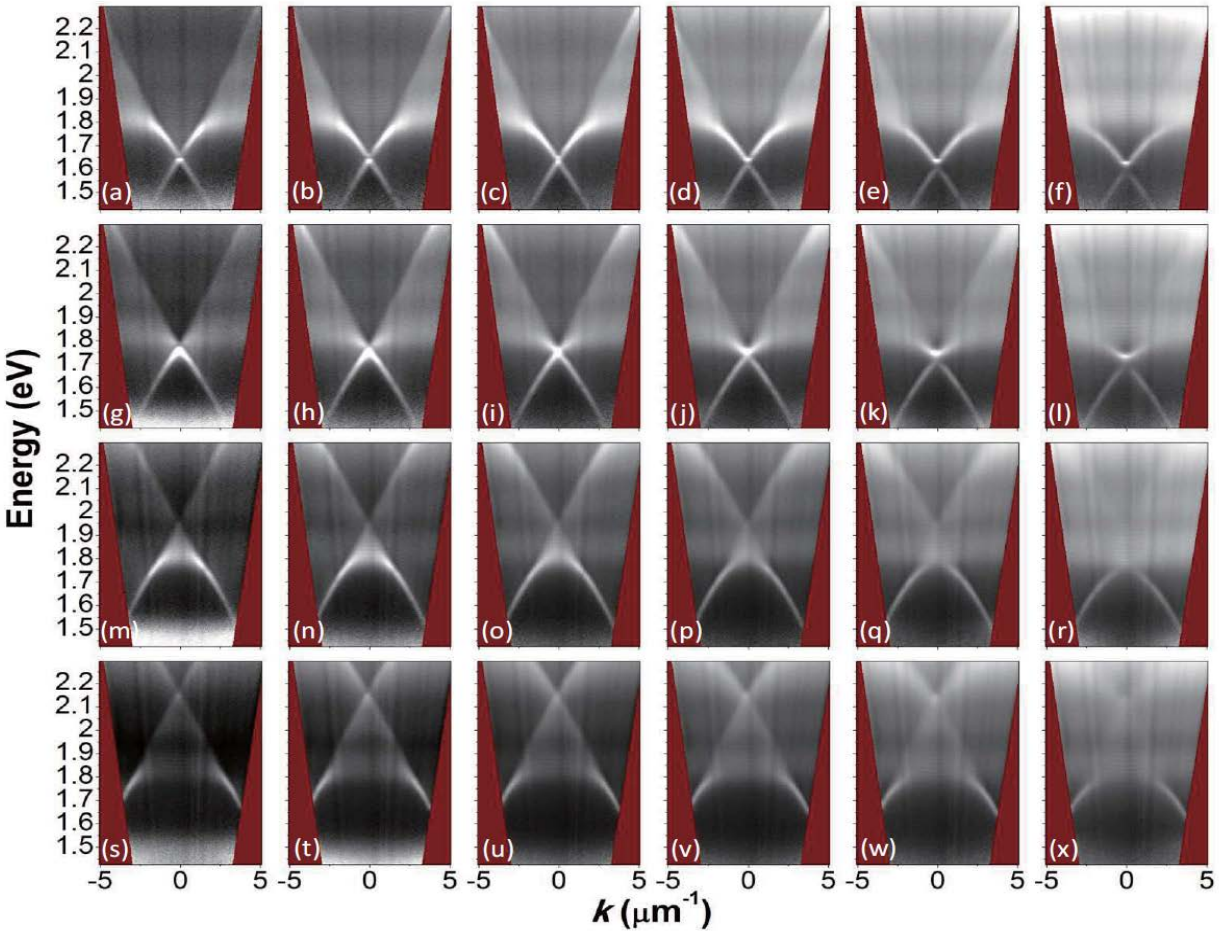

Fig. 11. The recorded raw extinction data for the arrays with 400 mM DiD concentration. The white (black) color corresponds to the highest (lowest) extinction.

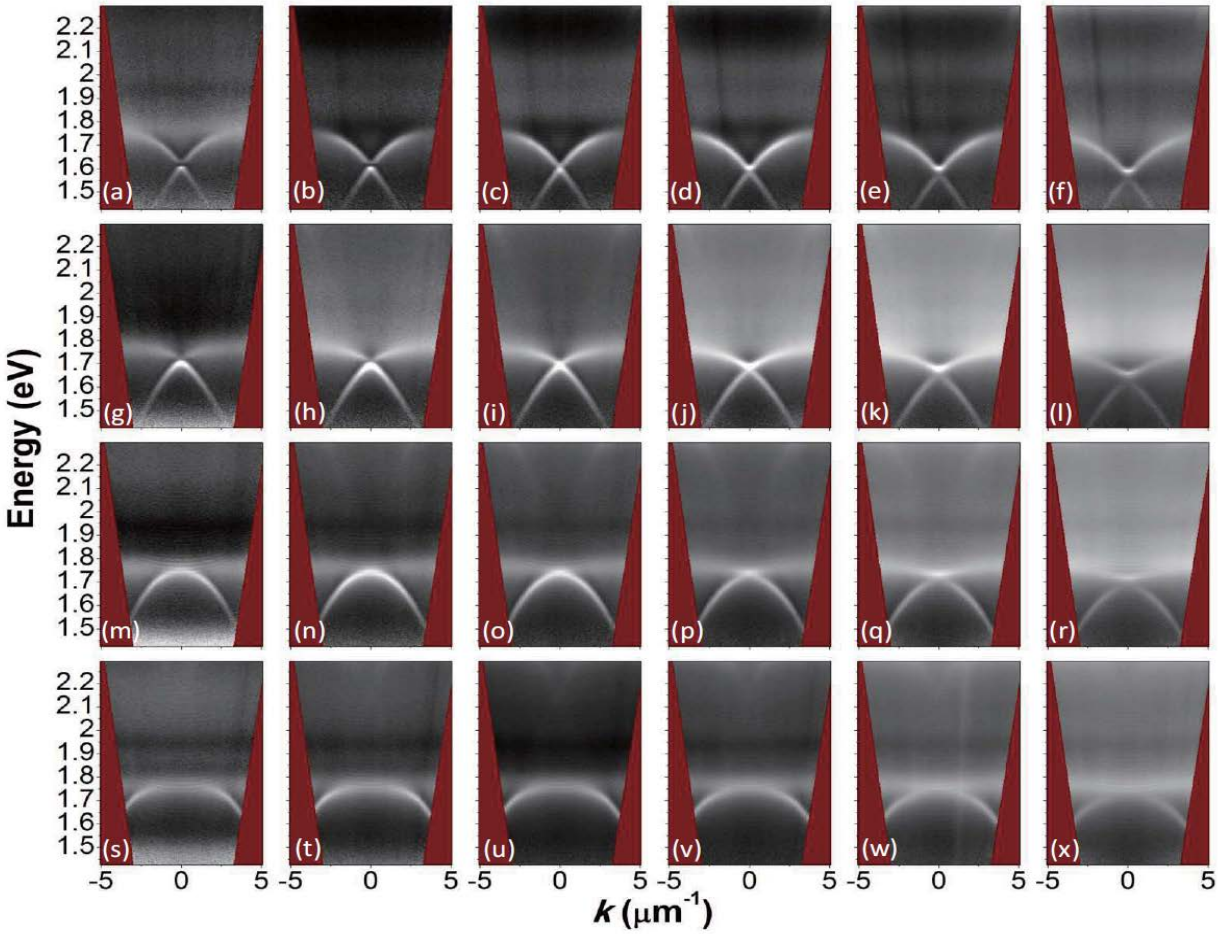

Fig. 12. The recorded raw extinction data for the arrays with 800 mM DiD concentration. The white (black) color corresponds to the highest (lowest) extinction.

The connection between the measured dispersion curves and the observed interference patterns

As pointed out in the manuscript, there exists an intimate connection between the measured dispersion curves and the observed spatial coherence images. In particular, one of the destructive interference fringes in the spatial coherence images always overlaps with the extinction maxima of the dispersion (yellow symbols), see manuscript Figs. 3 (a-d). This is because the spatially coherent light source (the sample) is radiating through a double slit. The slit effectively creates replicas of the original dispersion with equal spacing in k. The dark areas in the spatial coherence images correspond to the overlap region of the diffracted orders. However, in a strongly coupled system (for example with 400 mM and 800 mM DiD concentrations) the slope of the dispersion is reduced at large k-vector values, and the energy difference between the areas is reduced, making it harder to distinguish between the different orders. Figure 13 (a) illustrates this.

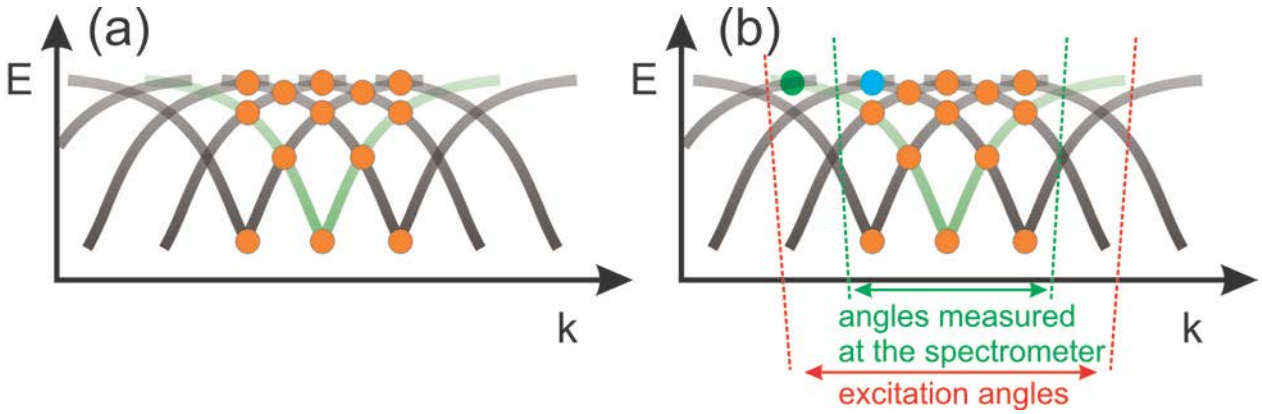

Fig. 13. (a) A schematic representation of the connection between the dispersion and the interference pattern. The double slit produces replicas (depicted as grey solid lines) of the original dispersion (depicted as green solid lines). The dark areas in the spatial coherence images correspond to the overlap region of the diffracted orders (here depicted as orange circles). In the strongly coupled system (400 mM and 800 mM concentrations) the slope of the dispersion is reduced at large k-vector values, and the energy difference between these areas is decreased, thus creating a complex interference pattern. (b) Some information is lost when generating an interference image from the measured dispersion due to the limited size of the CCD detector in the spectrometer: the angle distribution in the excitation light incident on the sample (depicted as red dashed lines) is larger than the range of angles that the spectrometer is able to measure due to the limited size of the CCD detector (depicted as green dashed lines). Thus some part of the incident light (such as the green circle), is still contributing to the measured interference image (the blue circle in the image) because it is effectively folded on a smaller momentum at the double slit plane, but it cannot be numerically reproduced from the measured dispersion data.

The effect creates a complex pattern in the interference image. To provide more information about the connection between the dispersion and the interference pattern, we numerically reproduced the interference images by (1) taking a fast Fourier transform (FFT) of the measured dispersion to obtain the real space distribution of the field after the sample, (2) used a spatial filter corresponding to the double slit (transmission = 1 at the spatial location corresponding to the slit openings and 0 elsewhere), and (3) performed an inverse FFT to the field transmitted by the double slit. In Fig. 14, the dispersion, the numerically generated spatial coherence image from the measured dispersion image, and the experimentally obtained spatial coherence images are shown for both 400 mM and 800 mM concentrations. The areas of destructive interference follow closely the extinction maxima of the dispersion (the yellow line). The numerically obtained interference patterns in Figs. 14 (b), (e) show slightly higher interference fringe contrast at high energies (1.75-1.8 eV) than the measured ones in Figs. 14 (c), (f). This is because certain high k vector values, although present in the interference experiment, Figs. 14 (c) and (f), are not present in the measured dispersions (see Fig. 13 (b)) due to the limited size of the CCD detector in the spectrometer, thus their contribution is absent in the numerically reproduced interference image. Importantly, the most prominent features of the measured spatial coherence images can be numerically reproduced from the measured dispersion image (describing the dispersion of the modes) radiating through a double slit. Thus we can conclude that the complex pattern in the spatial coherence image

originates from the interference of the strongly coupled delocalized mode (i.e. the measured dispersion) at the double slit.

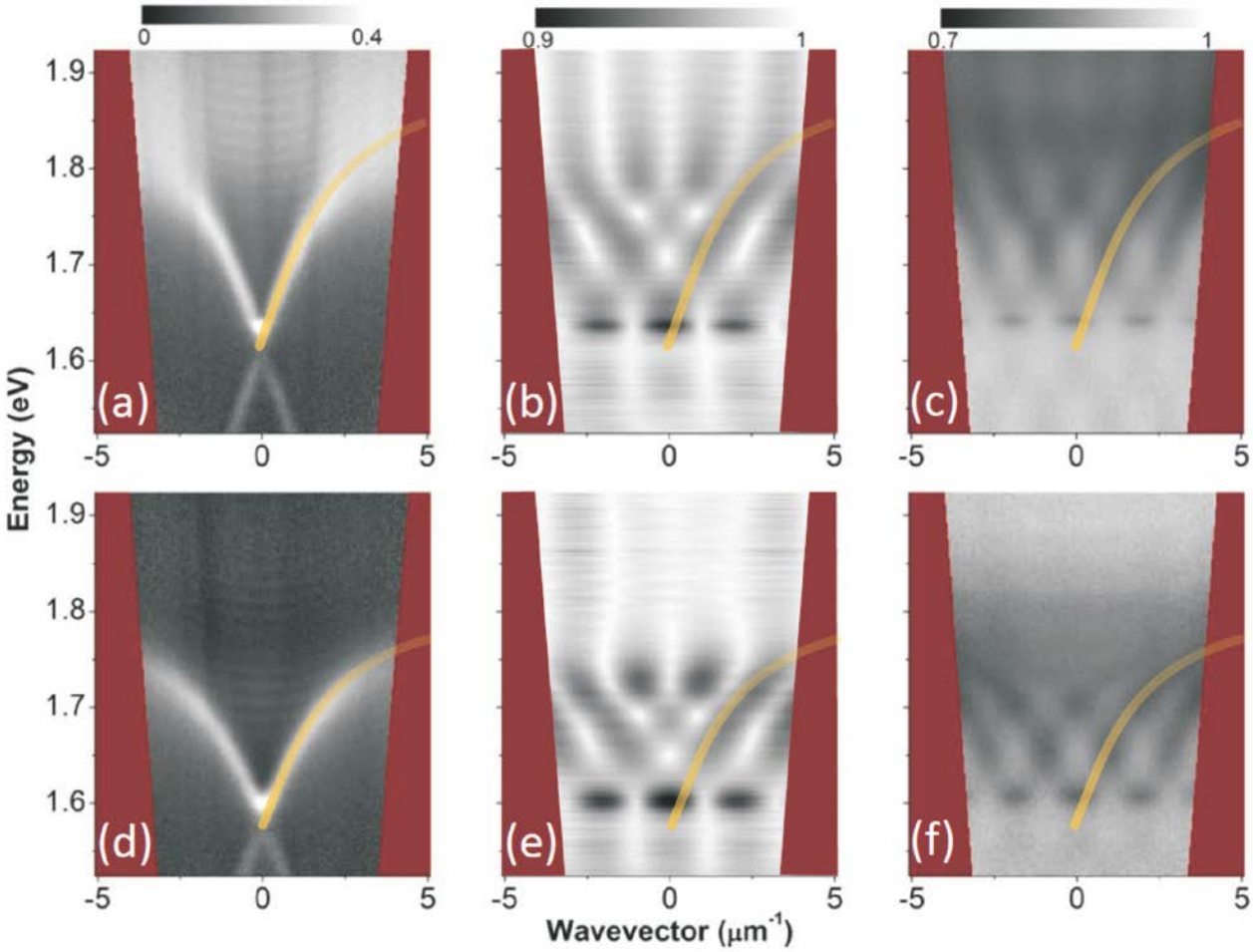

Fig. 14. (a) The measured dispersion, (b) the numerically generated spatial coherence image from the measured dispersion image, and (c) the experimentally obtained spatial coherence image for 400 mM DiD concentration. (d-f) The same for 800 mM DiD concentration. The yellow lines depict the extinction maxima of the dispersion curve. In the dispersions, we plot the extinction (1-T) as white color and for both spatial coherence images we plot the transmission T, as defined in the manuscript.

References

[1] V. M. Agranovich, M. Litinskaia, and D. G. Lidzey, Phys. Rev. B 67, 085311 (2003).

[2] A. Gonzalez-Tudela, P. A. Huidobro, L. Martin-Moreno, C. Tejedor and F. J. Garcia-Vidal, Phys. Rev. Lett. 110, 126801 (2013).

[3] R. A. L. Vallée, M. Van Der Auweraer, F. C. De Schryver, D. Beljonne, and M. Orrit, ChemPhysChem, 6, 81 (2005).